

pubs.acs.org/acsapm Article

Impact Velocity and Temperature Effects on the Shock Wave Propagation and Spallation of Hydroxyl-Terminated Polybutadiene: A Molecular Dynamics Study

Yuhao Liu, Jinlong He, Weikang Xian, and Ying Li*



Cite This: ACS Appl. Polym. Mater. 2023, 5, 8937–8948



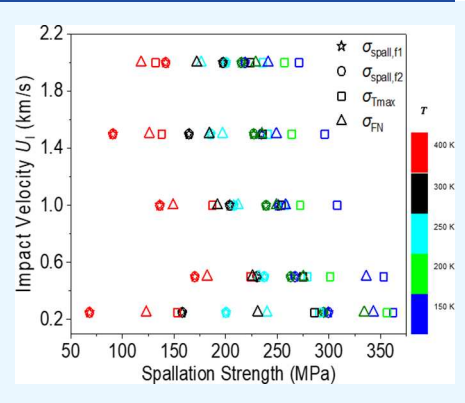
ACCESS I

III Metrics & More

Article Recommendations

Supporting Information

ABSTRACT: Hydroxyl-terminated polybutadiene (HTPB) is frequently employed as a key component of propellant binder in missiles or solid rockets. Understanding its shock response can help us to deepen our understanding of the shock response in its composites. Considering that missiles or solid rockets often need to operate in various temperature environments, investigating the shock wave propagation within the HTPB and its spallation behaviors under different temperatures and impact velocities is critical for understanding its failure modes. By employing large-scale molecular dynamics simulations, we provide a thorough analysis of the shock propagation and spallation strength of the HTPB under different initial temperatures and impact velocities. The quantification of the spallation strength is done by indirect methods based on the acoustic and modified acoustic assumptions and by the direct method that analyzes atomic stress in the spallation region. Our simulation results reveal that the spallation strength is associated with the impact velocity acting on the materials as



well as the initial temperature. When the initial temperature is below the glass transition temperature, the spallation strength exhibits a monotonic decrease with increasing impact velocity. In contrast, such monotonicity is not observed above the glass transition temperature. Our findings furnish insights at the molecular level regarding the spallation processes in HTPB under varying impact loadings and temperature conditions, thereby facilitating the design of HTPB materials with enhanced resistance to impact loading. KEYWORDS: hydroxyl-terminated polybutadiene, shock wave propagation, spallation strength, molecular dynamics simulations, temperature effect, impact loading

1. INTRODUCTION

Hydroxyl-terminated polybutadiene (HTPB) is extensively applied as adhesive, sealant, and propellant binder. 1-5 HTPB propellant, which serves as an energy source in solid rockets and missile systems, is comparatively less impact-resistant than the other components under dynamic loadings.⁶⁻¹¹ More specifically, the propellant is typically susceptible to various types of impact loadings, including launch overloads, accidental drops, and fragment impacts during attacks. 12 Suffering from the impact loading may result in the failure of the propellant, posing a substantial threat to the reliability of both rocket and missile systems, thereby compromising their effectiveness in operational scenarios. 13,14 Additionally, HTPB propellants often endure varying temperature conditions, such as the high-temperature environment generated during launch and freezing conditions in the Arctic region in winter. It is crucial to explore the mechanical response of HTPB, especially its failure modes under shock loading at different conditions because it is an important part of the composite propellant.

HTPB is a widely used polymeric binder in HTPB composites such as polymer-bonded explosives (PBX) and solid rocket propellants. Even though used in small fractions, the elastomeric binder absorbs much of the impact energy and

therefore requires careful modeling of its mechanical behavior to accurately simulate the response of HTPB composite, when they are subjected to large strains and strain rates. ¹⁵ For example, the main role of the polymer binder in PBX is to cushion the explosive crystals from mechanical insults such as vibration, impact, and friction. Therefore, knowing how shock wave propagates and how spallation happens within the HTPB material can help us understand the failure mode of its composite under impact, especially in the bonding interface with other materials. In addition, while most impact materials consist of HTPB composites rather than pure HTPB, there has been limited research dedicated to studying the impact behavior of HTPB composites using molecular dynamics (MD) simulations. This gap is primarily due to the intrinsic complexity of HTPB composites, which poses formidable

Received: June 19, 2023 Accepted: September 29, 2023 Published: October 12, 2023





challenges for detailed investigation with molecular resolution. Furthermore, existing research in this area is accompanied by methodological limitations. For instance, in the work of He et al., 16 the composite model of HMX/HTPB was constructed through simple stacking of individual components. This approach oversimplifies the structural complexities such that the composite's impact behavior might not be fully understood. Such limitations are amplified by the fact that HTPB composites inherently consist of cross-linked components, whose role in impact behavior cannot be understated. Therefore, there is no exact and systematic study of the impact response of HTPB composites. Besides that, it is still not clear how spallation occurs within its single component under impact. In our research, we primarily focus on examining the impact behavior of pure HTPB, a major element of HTPB composite materials. We aim to understand the impact response of the HTPB element when it is part of the HTPB composites. Understanding the impact dynamics of this singular component is vital before progressing to a comprehensive study of HTPB composite materials.

Recent studies on HTPB have primarily centered around its mechanical properties, like tensile strength, Young's modulus, and complex moduli. These properties have been investigated by changing the ratio of its constituents or mixing with other materials, forming composites under quasi-static or dynamic loading conditions. Mahottamananda et al. showed that HTPB blended with paraffin wax in various weight ratios leads to significant improvements in maximum stress and Young's modulus while slightly decreasing elongation.¹⁷ Sekkar et al.¹ virtually synthesized HTPB-based urethane networks using various stoichiometric ratios and established a correlation between calculated network parameters and mechanical properties, demonstrating that the R value (equivalent ratio of -OH by that of -NCO groups) influences the storage moduli, but not for loss moduli. Jordan et al. 19 systematically characterized isocyanate-cured HTPB properties with varying plasticizers, revealing that an increase in plasticizer content reduces the material strength. Using split Hopkinson pressure bar (SHPB), Chen et al.²⁰ explored the properties of HTPB with different strain rates (700-2000 s⁻¹) under compression, establishing that higher strain rates increase modulus and compressive strength while maintaining viscoelasticity. Hengning et al.²¹ also used the SHPB apparatus to explore the dynamic behaviors of HTPB propellants under varying strain rates $(10^3-10^4 \text{ s}^{-1})$. Their findings indicate that the strain rate heavily influenced key mechanical characteristics, such as strain energy and ultimate strength. Dynamical compression tests on HTPB polymer and its composite conducted by Sunny et al.²² demonstrated a transition in the polymer's rate sensitivity and suggested a decrease in rate sensitivity in the HTPB composite under the strain rate of 2100 s⁻¹. Yang et al.²³ conducted thorough compression testing on HTPB propellant at varying strain rates $(1.7 \times 10^{-4} - 2500 \text{ s}^{-1})$ at room temperature, indicating a linear increase in stress with strain at each condition. Only a few studies focus on investigating the response of HTPB subject to impact loading. Markus et al.²⁴ discovered that the shear stress near the shock front dissipates within approximately 0.5 ps while a glass-like state takes place, leading to a notable increase in structural relaxation times. Investigations into two HTPB compositions by Millett et al.² using manganin stress gauges revealed a linear shock velocityparticle velocity relationship, with a lower value of acoustic speed observed for the composition with higher plasticizer

content, suggesting the plasticizer enhances material compliance.

To our knowledge, no available research has been found regarding the spallation strength of HTPB material under impact loading, particularly using molecular simulation (MD) to calculate the spallation strength of HTPB at different temperatures and impact loadings. Spallation strength is an important indicator of material failure under impact loading.26 Therefore, understanding the spallation strength of HTPB under various temperatures and impact loadings could assist in design that improves the shock resistance of the materials. Over the past few decades, MD simulation emerging as an influential method has been used to investigate the thermal, mechanical, and dynamic properties of material systems comprehensively which allows researchers to gain valuable insights into the atomistic and molecular aspects of the studied system.²⁷ Nonequilibrium MD methods can be used to explicitly model the transmission of shock waves under impact loading, which can help reveal spallation strength information directly. It has been commonly employed to study the impact response and the occurrence of spallation in both ceramics 28,29 and metals. 30,31 Furthermore, by utilizing the velocity history of the free surface extracted from MD simulations, we can calculate the spallation strength by two different indirect methods. These methods, based on the acoustic assumption, are commonly used in experiments to measure the spallation strength of materials under impact loading because it is difficult to directly measure the spallation strength of materials under impact loading without altering the material properties. We conducted a comparison of the spallation strength of the HTPB sample using the indirect methods and direct methods.

This paper is structured in the following manner: Section 2 introduces the computational model we used with validation of the interatomic potential. Methods used to study the spallation strength of HTPB and Hugoniot data are also presented. In Section 3, the calculated Hugoniot data using multiscale shock simulation technique (MSST) and following analysis based on results of MD simulations are detailed. Section 4 is a summary of our findings from this study.

2. COMPUTATIONAL MODEL AND METHODS

We employed the Large-scale Atomic/Molecular Massively Parallel Simulator (LAMMPS)³² to perform MD simulations and OVITO³³ for visualization. The polymer consistent force field (PCFF)³⁴ were used to model the HTPB polymer because it offers more precise atomic charges and van der Waals parameters, enabling accurate modeling of surface and bulk properties.³⁵

2.1. Benchmarking: Static and Dynamic Properties of *cis***-1,4-Polybutadiene Melts.** We selected *cis***-1,4-PB** as a surrogate model for HTPB benchmark was performed to ensure that the model reproduces the structural characteristics of the polymer backbone. The benchmark includes a comparison of mean-square radius of gyration $(\langle R_g^2 \rangle)$, mean-square end-to-end distance $(\langle R^2 \rangle)$, specific volume (ν) , characteristic ratio (C_n) , total structural factor (S(q)), and radial distribution function (g(r)). These properties quantify the static structural information on the material. The corresponding figures have been included in the Supporting Information.

The specific volume (ν) is a bulk property that can be used to directly compare with experimental date.^{37,38} It is influenced by the chain length of the polymer. In Figure S1 of the

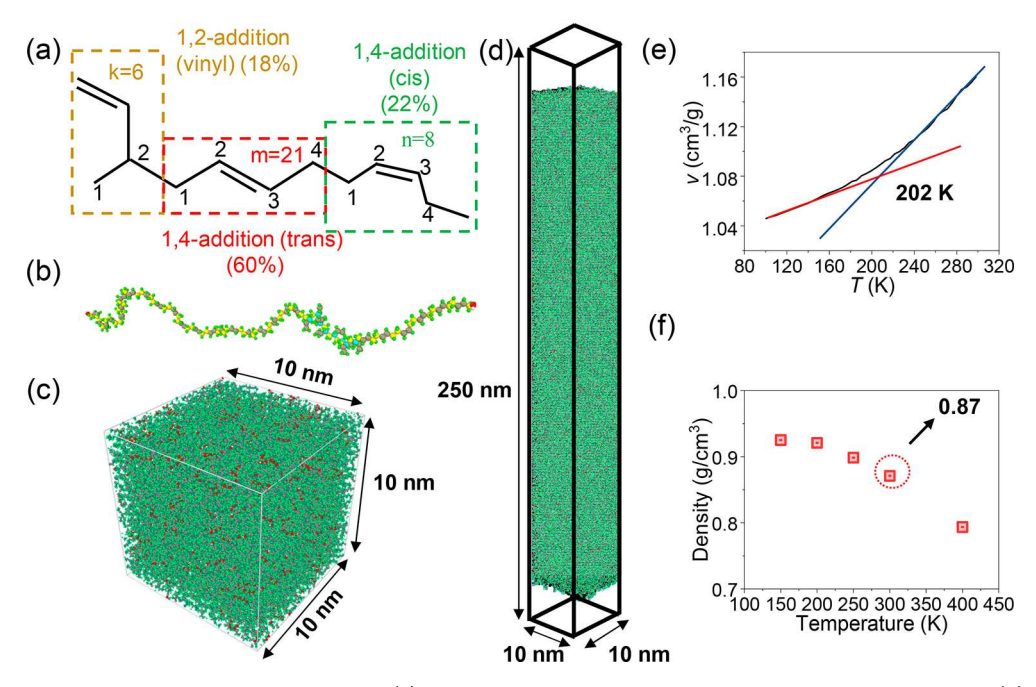


Figure 1. Modeling and validation of HTPB polymers: (a) Chemical structures of hydroxyl-terminated polybutadiene. (b) A typical HTPB polymer chain. (c) Snapshot of the MD model in $10 \times 10 \times 10$ nm³ that contains 296 chains used for MSST. (d) Model in $10 \times 10 \times 250$ nm³ that contains 1776 chains used for shock simulation. (e) Estimation of the glass transition temperature. (f) Change of the density.

Supporting Information, we present the values of v for cis-1,4-PB melts as a function of the chain length (N), which is fitted by

$$v = v_{\infty} + \frac{v_0}{N} \tag{1}$$

where v_{∞} is the specific volume in the case of extensively long chain. The constant v_0 characterizes the effect of the chain length (N). The fitting yields $v_{\infty} = 1.26$ cm³/g and $v_0 = 2.76$ cm³/g. Garrett et al.³⁶ documented values of $v_{\infty} = 1.2225$ cm³/g and $v_0 = 2.61$ cm³/g.

The structure factor we calculated is shown in Figure S2, displaying two peaks. One is near 1.4 Å⁻¹ related to the interchain correlations and partially influenced by the interaction among intrachain monomers. The other, near 3 $Å^{-1}$, results from the covalent bond along the chain backbone. Two peaks are shown in experimental measurement.³⁹ Besides, g(r) is also extracted. Figure S3 presents the g(r) as N changes and the comparison with the results simulated by Tsolou et al.40 The first noticeable peak, indicative of the average position of the initial intermolecular neighbors, is perceived at an approximate distance of 5.8 Å. Simultaneously, the second peak is positioned roughly at 10.3 Å. Both peaks appear at positions nearly identical to the result simulated by Tsolou et al.40 The comparison suggests that our model captures the essential characteristics of the intermolecular and intramolecular interactions of HTPB.

The structural characteristics of the carbon backbone in a single chain can be quantified by calculating the $\langle R_g^2 \rangle$ values

$$\langle R_{g}^{2} \rangle = \left\langle \frac{\sum_{i=1}^{n} m_{i} (r_{i} - r_{\text{CoM}})^{2}}{\sum_{i=1}^{n} m_{i}} \right\rangle$$
 (2)

where *i* denotes the index of an atom, while *n* symbolizes the cumulative count of atoms. m_i is representative of the mass attribute of a solitary atom, whereas r_i symbolizes the position vector of a single atom. Furthermore, r_{COM} signifies the position

vector of the gravitational center of the system. The calculated value of $\langle R_{\rm g}^{\ 2} \rangle$ is reported in Table S1. The calculated results from the work of Garrett et al.³⁶ are also given in the same table, which shows a close agreement.

The relationship between $\langle R^2 \rangle$ and molecular weight was analyzed. Both our study and the research by Garrett et al.³⁶ have been depicted in Figure S4. Our slope, measured at 0.91 Å² mol g⁻¹, closely aligns with the 0.85 Å² mol g⁻¹ observed by Garrett et al.³⁶ In understanding the PB melt model's physical reasoning, we introduce the parameter C_n :

$$C_n = \frac{\langle R^2 \rangle}{4n_{\text{mer}} l^2} \tag{3}$$

In this equation, n_{mer} denotes the comprehensive count of monomers in a single chain. l^2 represents the mean-squared extent of the skeletal bond. The C_n values calculated in this study are presented in Figure S4. The C_n for an infinitely long chain, represented as C_{∞} , was derived from the equation

$$C_n = C_{\infty} + \frac{C_0}{n_{\text{mer}}} \tag{4}$$

where C_0 signifies the rate at which it changes based on the monomer count in a single chain. In our study, C_0 is -10.6 (N) and C_{∞} is 5.4. These are similar to Garrett et al.'s values of -9 (N) and 5.5. A comparison, including a fitting figure, is given in Figure S5.

2.2. Construction of Atomistic HTPB Models. HTPB is a kind of polymer with hydroxyl functional groups present at both ends of the polybutadiene chain. It can be synthesized through radical polymerization. During the polymerization process, the butadiene monomers can add to the growing chain through three different addition modes: 1,2-addition, 1,4-addition (*cis*), and 1,4-addition (*trans*) (refer to Figure 1a). The addition modes contribute to the final polymer structure and their ratios can affect the final properties of the polymer. In this research, the ratio of commercial HTPB-QL (1,2-vinyl/

1,4-trans/1,4-cis = 0.18/0.60/0.22) was used to build our MD model. A single HTPB chain, as shown in Figure 1b, consists of 8 repeating 1,4-cis segments (n=8), 21 repeating 1,4-trans segments (m=21), and 6 1,2-vinyl segments (k=6) such that the molecular weight is 1924 g/mol. It is worth noting that this molecular weight closely aligns with the entangled molecular weight ($M_{\rm e}$) typically reported in the literature, which falls within the range of approximately 1500–2300 g/mol, as documented in ref 43. This agreement with established values further reinforces the relevance and reliability of our simulation setup in representing real-world polymer behavior. Consequently, the materials are expected to exhibit a "thick" liquid state with varying viscoelastic properties at different temperatures.

Figures 1c and 1d show the constructed MD models for the MSST and shock simulation, respectively. The MSST approach was originally introduced by Reed et al.44 as a multiscale MD technique that satisfies both shock Hugoniot and the Rayleigh line to compute Hugoniot data at a reduced computational cost. 45 The MSST method is based on the 1D Euler equations for compressible flow. These equations represent the conservation of mass, momentum, and energy throughout the wave. MSST enables the simulation of the atomistic behavior of the shock front using a smaller model for a shorter duration. 46,47 We have compared the computational costs between nonequilibrium MD simulation and the MSST method. For example, with an impact velocity of 2 km/s and an initial temperature of 300 K, we calculated the impact process to last 120 ps using the MD simulation. This simulation took 154 h and 42 min with 180 CPU cores (5 nodes). In contrast, the MSST method took only 10 h and 11 min using 36 CPU cores (1 node). The communication cost is 14% and 9% of total computation time for MD simulation and MSST, respectively. The computation was conducted in the national renewable energy laboratory (NREL) high-performance computing (HPC). The CPU configuration used in those simulations is dual-intel xeon gold skylake 6154. Besides that, MSST helps us calculate the longitudinal acoustic speed in the MD model for later determination of spallation strength using indirect methods. The HTPB sample that has dimensions of 10 \times 10 \times 10 nm³ and a total of 296 chains was implemented in LAMMPS to model the thermodynamic states behind the shock wavefront using MSST. The cubic HTPB sample is subjected to impact loading in the z-direction. Hugoniot data were computed at 5 different temperatures (150, 200, 250, 300, and 400 K) and impact velocities (0.25 0.5, 1, 1.5, and 2 km/s). In total, 25 computations conducted. As an equilibrium method, the MSST focuses on the initial and final state of material under impact, instead of characterizing the complete impact process. In this study, the MSST method serves two purposes. First, we use it to benchmark the results from MD simulations, specifically for data like shock velocity (U_s) . We can extract this information from both methods, which is discussed in Section 3.2. Second, by fitting the $U_{\rm s}$ - $U_{\rm p}$ (particle velocity) curve using the equation $U_s = C_b + SU_p$, we can calculate the bulk sound speed (C_b) and its slope value (S). This information assists us in determining the spallation strength through two indirect methods, allowing us to compare the spallation strength derived directly from MD simulations with that obtained from indirect methods.

Alternatively, nonequilibrium classical MD simulations are employed to explicitly simulate the shock wave propagation and to study the spallation mechanism explicitly. Another model system with box size of $10 \times 10 \times 250$ nm³ containing 1776 chains was used to directly simulate the shock waves propagation from which we can obtain the Hugoniot states behind the shock front with different impact velocities and temperatures. It is worth noting that vacuum spaces are set at the ends along the z direction, as shown in Figure 1d, while the inner HTPB volume of the simulated box varies with different temperatures.

The MD model of HTPB was constructed using the selfavoiding random walks approach. The polymer equilibration process was conducted five times at different temperatures while the atmospheric pressure. To illustrate how the system was equilibrated, we will focus on the model at 300 K. Initially, the overlapping atoms in the initial system were separated by performing energy minimization based on the conjugate gradient criterion. Subsequently, the system was initially permitted a relaxation phase lasting for 3 ns using the isothermal-isobaric (NPT) ensemble at room temperature (300 K) and atmospheric pressure (1 atm). This was followed by an additional relaxation period of 3 ns in the canonical (NVT) ensemble at the same temperature. To alleviate any potential residual thermal stresses in the system, a sequence of 10 annealing cycles was conducted. During each cycle, the system's temperature was increased from room temperature to 1000 K over a time span of 3 ns. The temperature was then maintained at 1000 K for 3 ns to allow for relaxation and finally cooled back down to 300 K over the subsequent 3 ns. After the annealing cycles, the system underwent an additional relaxation process for 3 ns in the NPT ensemble under room temperature (300 K) and atmosphere pressure (1 atm), followed by an additional 3 ns relaxation using the NVT ensemble, maintaining room temperature. During the equilibration simulations, a time step of 1.0 fs was used. Before initiating the production simulation, an extra relaxation phase of 5 ns was conducted under the NVT ensemble at 300 K. During the entire equilibration process, periodic boundary conditions were implemented in the x, y, and z directions while maintaining atmospheric pressure at three principal directions.

Figures 1e and 1f illustrate the variation of the specific volume and density, respectively, at different temperatures. The glass transition temperature (T_g) and density are crucial indicators for validating the effectiveness of computational models, particularly in the field of polymer and materials science. ⁴⁸ The density of HTPB was determined by averaging the density over the last 1 ns of the equilibration period. The transition in the slope value of the specific volume curve is indicative of the $T_{\rm g}$ of the HTPB sample.⁴⁹ Dossi et al.^{41,50} conducted experiments to measure the T_{σ} of commercially available HTPB, which was found to be 197 K. Our MD model yields 202 K, with a 3.0% difference compared with the experimental data. The density of commercial HTPB has been reported by Zhou et al.⁴² to be 0.90 g/cm³ at 300 K. Our model shows a density of 0.88 g/cm³, with a 3.3% difference. As shown in Figure 1f, the density of the HTPB sample increases with a decreasing temperature. The density does not change much when the temperature drops below the T_o because the chains becoming more tightly packed and exhibiting limited mobility in the glassy state.

Besides that, the difference between pure HTPB and HTPB composites when temperatures fall below $T_{\rm g}$ should be discussed. In HTPB composites, the behavior below $T_{\rm g}$ can be glassier and brittle, and therefore the molecular mobility of the chains is restricted. However, the relaxation time of the

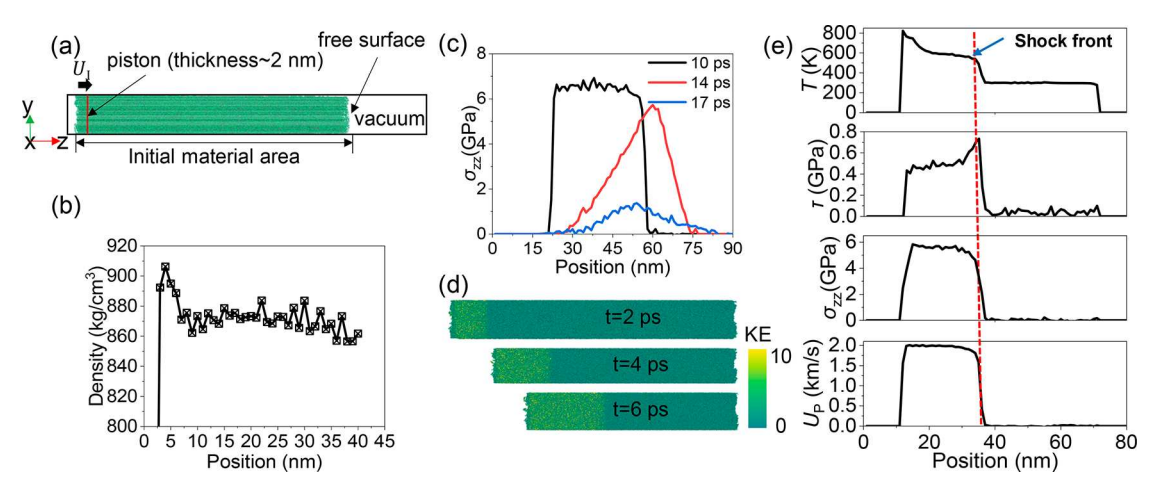


Figure 2. Side view of the HTPB sample used to model shockwave propagation and the variations of thermodynamic quantities along the length of HTPB: (a) a side view to model shockwave propagation, (b) the variation of density along the z direction (300 K), (c) the variation of normal stress with the impact velocity of 2 km/s at three times (300 K), (d) the snapshots of shock propagation with the impact velocity of 2 km/s, where the colors of particles represent their kinetic energy (300 K), and (e) the change in thermodynamic quantities along the length of HTPB sample at 6 ps (300 K).

pure HTPB chains, estimated using the Rouse model, is approximately 20 ns. In our study, the simulated impact time is 110 ps maximum. As a result, the impact process used in our study may not have a sufficient duration to allow for the complete relaxation of the polymer chains. Thus, we contend that any potential effects arising from chain mobility are likely to exert only a minor influence on the results presented in this article.

2.3. Shock Wave Propagation by MD Simulation. We apply impact loading to the HTPB model by displacing a slab of atoms, defined as the piston, along the z direction of the box, as shown in Figure 2a. The piston has been commonly employed in MD simulations to simulate the shock wave propagation.^{29,52} In this method, we increase the velocity of the atoms in the piston area to match $U_{\rm I}$, mimicking external impact loading acting on the sample. Consequently, a shock front is generated at a velocity known as the shock velocity, denoted as U_s . For impact velocities of >1.5 km/s (specifically, 2 km/s in this paper), the piston moved within the sample for 10 ps. However, for impact velocities of 0.25 0.5, 1, and 1.5 km/s, the piston was moved for 20 ps. These durations were chosen to make sure that the moving piston does not encounter the reflected wave, thus generating a stable shock front. To analyze the changes in thermodynamic variables along the impact direction, the simulation region was partitioned into narrower z direction bins, each spanning a width of 1 nm. The thermodynamic properties relevant to each bin were spatially averaged and then time-averaged over 100 timesteps at intervals of 200 timesteps. The shock simulations utilized a time step of 0.1 fs. In Figure 2b, the spatial variation of densities at a certain time is shown where a slightly reduced density, because of the free surface, near the right end is observed. A similar result was also documented in the work of Dewapriya et al., where reduced density near the free surface was observed in their models of polyurethane and polyurea structures.⁵³

3. RESULTS AND DISCUSSION

3.1. Hugoniot Data Computed by MSST. Figure 3 plots the particle velocity values (U_P) and shock velocity values (U_s) at different initial temperatures. Linear fittings are applied to

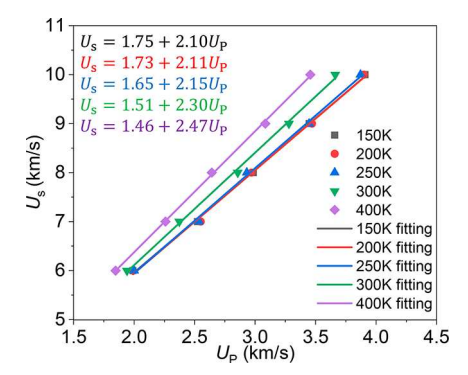


Figure 3. Calculated Hugoniot data of HTPB using MSST: shock velocity $U_{\rm s}$ versus particle velocity $U_{\rm p}$.

the data. It is worth mentioning that prior studies ^{19,25,53} have also demonstrated a linear correlation between the particle velocity and the shock velocity, as represented by the equation

$$U_{\rm s} = C_{\rm b} + SU_{\rm p} \tag{5}$$

where $C_{\rm b}$ represents bulk sound speed and S is the slope value of the fitting curve. Those fitting data can be used for later calculations of the indirect spallation strength of the HTPB material. Especially, Jordan et al. bottained a linear relationship of $U_{\rm s}-U_{\rm p}$ for the impact of HTPB material at 300 K by fitting experimental data with $C_{\rm b}=1.57$ km/s and S=2.17 while we found that $C_{\rm b}=1.51$ km/s and S=2.30. Although Jordan et al. dded about 10% plasticizer into the HTPB. Because the amount of plasticizer they added to the pure HTPB material is quite low relative to the HTPB itself, we believe that this comparison is meaningful.

We also note that C_b increases as the temperature decreases while S decreases when the initial temperature is above the T_g . A higher value of C_b and a lower value of S indicate greater impact resistance of the materials. However, as the temperature decreases below T_g , changes of C_b and S are irrelevant because of the transition of the material to a glassy solid state. As indicated in Figure 1f, the polymer density increases significantly when the initial temperature of the HTPB material is above the T_g . Previous research from Linder

et al.⁵⁴ has also demonstrated a strong correlation between the speed of sound propagation in a material and its density.

3.2. Shock Wave Propagation. Figure 2d shows snapshots of the shock wave propagating where the color in the figure represents the value of kinetic energy changed by the shock wave. Hence, the kinetic energy can be used to track the shock wave propagation from the left to the right ends of the simulation box. The quantities of interest at t = 6 ps are shown in Figure 2e. The temperature near the piston shows a maximum value and then decreases when near the shock front but remains the same as the initial values in the area where the shock wave did not propagated. The shear stress in this paper is defined as 55,56

$$\tau = \frac{1}{2} \left(\sigma_{zz} - \frac{\sigma_{xx} + \sigma_{yy}}{2} \right) \tag{6}$$

where the σ_{xx} σ_{yy} and σ_{zz} represent the stress components in the principal directions. They can be extracted from the simulation directly. The shear stress increases only slightly from the piston position but increases significantly at the position near the shock front, until the peak value is reached at the shock front. In contrast, σ_{zz} demonstrates an almost opposite trend. It shows a slight decrease from the piston location to the location of the shock front and then suddenly drops as it approaches the shock front. The particle velocity $U_{\rm P}$ remains relatively constant and does not change significantly with location in passed area of shock wave.

The change of normal stress σ_{zz} as a function of time provides overviews of the entire impact process. Figure 2c shows the profiles of σ_{zz} at three different moments. These three moments respectively correspond to three important stages during the propagation of shock waves. 10 ps represents the moment when the piston has just been released, while the shock wave has not yet arrived at the right edge. 14 ps is the moment when the release wave generated for the released piston meets the reflected wave produced after the shock wave arriving at the rightmost edge of the material. The profile at 17 ps shows stress state after the two waves meet. Before the release wave and the reflected wave meet, σ_{zz} is maintained between the two waves. When the two waves meet with each other, the normal stress presents the maximum value at the meeting position. After the two waves meet, σ_{zz} gradually dissipates from the position where they meet. Figure 4a depicts the complete evolution of the normal stress. Particularly, the shock wave just reached the right boundary of the bulk of the material at 12 ps. Dissipation of σ_{zz} was observed after 14 ps as a result of the interference of the release and the reflected

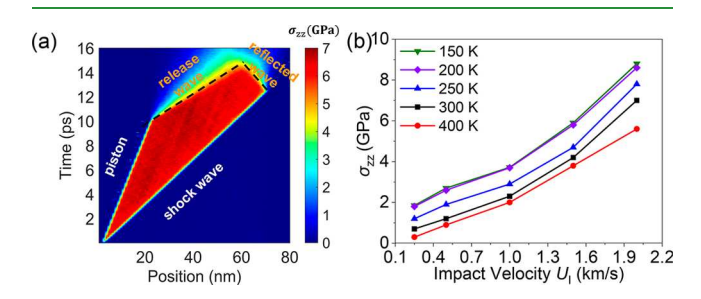


Figure 4. Normal stress σ_{zz} accessed from the explicit MD simulation: (a) the time-dependent profile of normal stress σ_{zz} under the impact velocity of $U_{\rm I} = 2$ km/s at 300 K; (b) the change of maximum normal stress σ_{zz} as under different conditions.

waves. In addition, the movement of the shock front is represented by the marked straight line in Figure 4a, and the inverse of its slope denotes the shock velocity (U_s) . U_s is 5.83 km/s in this case. As predicted by the shock Hugoniot curves obtained by MSST from Figure 3, the computed U_s is 6.11 km/s. The difference between the MD simulation and the MSST simulation is around 4.5%. In addition, the maximum values of σ_{zz} under different combinations of impact velocities and initial temperatures have also been extracted as shown in Figure 4b. As a quantity that can be directly measured in experiments, σ_{zz} can be used to verify the accuracy of presented method about which the discussion will be given in Section 3.5. In Figure 4b, with the increase in $U_{\rm I}$, the maximum σ_{zz} significantly increases because the increase in $U_{\rm I}$ results in higher energy. However, as the initial temperature increases, the maximum σ_{zz} decreases. On the other hand, when the initial temperature is under the $T_{g\prime}$ the maximum σ_{zz} seems independent of the temperature. The temperature independence and dependence are attributed to the changes mass density at different temperature, as the density can affect the energy transfer efficiency.⁵⁷ As previously discussed in this paper, when the temperature is under T_g , it has little effect on the density but changes the density significantly when it is above the T_g .

3.3. Shock-Induced Spall Fracture. The density information on a material directly reflects its continuity. Therefore, the density of a material can be used as an indicator to determine whether spallation occurs under impact. Figure 5a presents the density profile of the material under four different impact velocities at 300 K. To avoid interactions with reflected waves, the piston was gradually moved within the sample over a duration of 20 ps, considering the relatively low impact velocities utilized in these simulations. As shown in Figure 5a, as $U_{\rm I}$ increases, the spallation of the HTPB sample becomes more pronounced, starting from being hardly noticeable in the case of $U_1 = 0.25$ km/s to being clearly visible in the case of higher impact velocities. The transition is demonstrated in Figure 5b where snapshots at 70 ps are shown. A similar trend was reported in the MD simulations by Dewapriya et al., 53 despite they use different materials.

Figure 6a depicts the spatial and temporal changes in tensile stress in the HTPB polymer under an $U_{\rm I}$ of 0.5 km/s with the initial temperature of 300 K. The profiles of the tensile stress $\sigma_{\rm T}$ align closely with the density profiles shown in Figure 5a. Figure 6b, a zoomed-in version of Figure 6a, presents the tensile stress $\sigma_{\rm T}$ at the initial moment and position of spallation. The highlighted area indicates approximately the initialization of the spallation.

Figures 6c and 6d illustrate the changes in maximum tensile stress at different locations and at different moments of impact over time, respectively. As can be observed from these figures, the maximum tensile stress roughly occurs at the 35–55 ps timing of impact within the 40–60 nm range of the sample. This coincides with the position and time of spallation occurrence, as shown in the time—position evolution of the density graph for the HTPB sample, suggesting that tensile stress could be the direct cause of failure in HTPB materials during the shock process.

The maximum tensile stresses at different locations ever experienced during the whole simulation process were recorded, and the results are shown in Figure 6c. In Figure 6d, the maximum tensile stresses, regardless of the position, are shown against the time. From the results in Figure 6, the

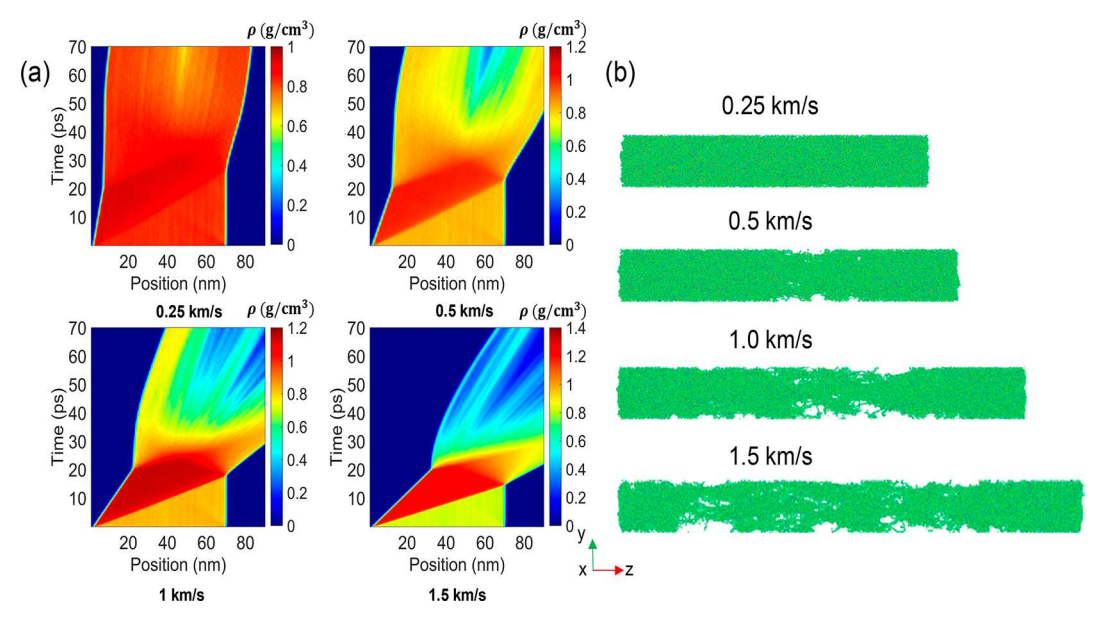


Figure 5. Investigation of the spallation behavior of HTPB under different conditions: (a) time-dependent density profiles under different impact velocities $U_{1\bar{1}}$ (b) snapshots of the simulations at 70 ps.

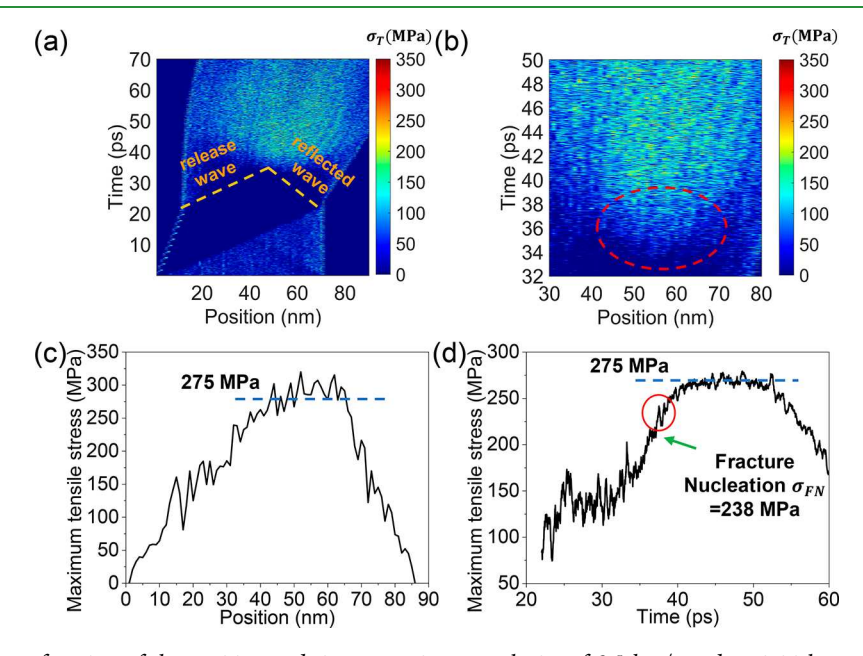


Figure 6. Tensile stress as a function of the position and time at an impact velocity of 0.5 km/s and an initial temperature of 300 K: (a) the complete profile, (b) zoomed-in view of (a) with the highlighted area as the estimated location where the spallation initializes, (c) spatial changes in the maximum tensile stress, and (d) the change of the highest tensile stress over time (the curve is graphed using a moving average method). The dashed horizontal line marks the average highest tensile stress, and the arrow points to the onset of tensile failure. The relevant figures when the impact velocity is set at 0.5 km/s.

maximum tensile stress approximately occurs within the 40 to 60 nm area from 35 to 55 ps, and it coincides with the position and time of spallation occurrence as shown in density profiles shown earlier, suggesting that the change of the density and thus the spallation of the material are directly related to the tensile stresses. It is worth noting that a cluster average was applied to acquire the data shown in Figure 6d to filter the fluctuations caused by the fact that the data was record every time step.

It is worth noting that in Figure 6d we applied a moving average to the data in the graphic. This is because we extracted data every 0.1 fs. Without processing, the graph would exhibit

significant fluctuations, making direct observation challenging. After processing, it was found that the average values at the locations of maximum tensile stress in Figures 6c and 6d are identical. We define this value as the maximum tensile strength of the HTPB material, denoted in this paper as $\sigma_{T_{\rm max}}$. A comparison between Figures 6c,d, and Figure 5a reveals that material failure, or spallation, occurs when the maximum tensile strength is reached. In engineering practice, using this value as the spallation strength of the material makes it difficult to provide early warnings of material failure. Consequently, we have redefined a smaller tensile strength, namely, the "fracture nucleation stress", denoted as $\sigma_{\rm FN}$. The point at which fracture

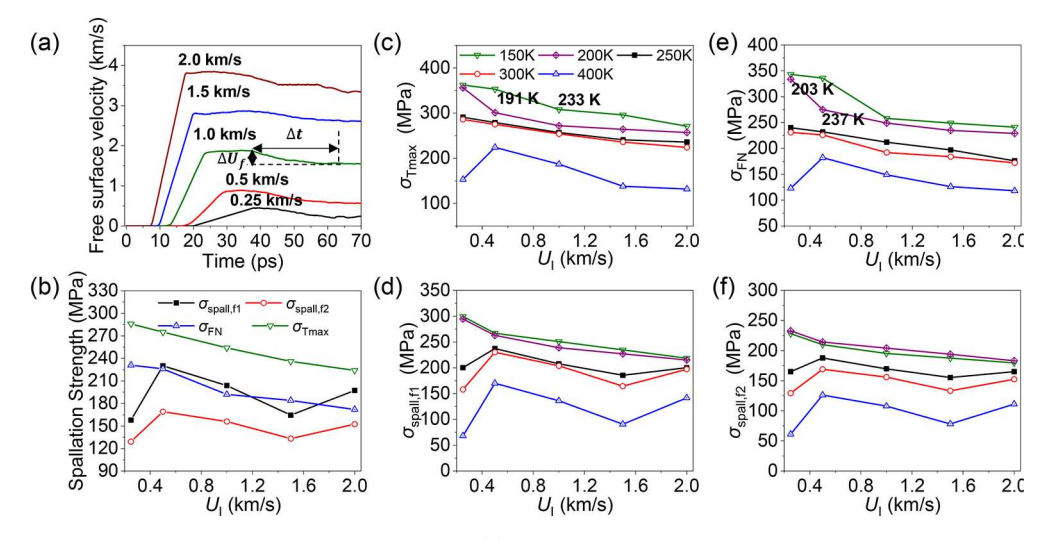


Figure 7. Variation in free surface velocity and spallation strength. (a) Changes in free surface velocity over time under various impact velocities. (b) Variation in four types of spallation strengths in relation to impact velocities at an initial temperature of 300 K and the variation of four kinds of spallation strengths with impact velocity at different temperatures: (c) maximum tensile stress, (d) fracture nucleation stress, (e) first acoustic approximation, and (f) modified acoustic approximation. The temperatures inserted in (c) and (d) indicate the average temperature at the spallation location within the samples.

initiation occurs, or the fracture nucleation point, can be identified by examining the temporal changes in the maximum tensile stress within the sample. The occurrence of a sudden increase in the tensile stress, corresponding to the intersection of two unloading waves, indicates the onset of fracture (as indicated in Figure 6d). We have characterized the nucleation stress as the mean tensile stress over a period of approximately 1 ps following the onset of fracture nucleation. However, it is evident that some declines exist prior to the defined area of "fracture nucleation". The reason these areas are not labeled as such can be inferred from Figure 5a. At an impact velocity of 0.5 km/s, the spallation area is located between 50 and 60 nm during the 30–50 ps time frame. While declines are observed before this defined area, no spallation occurs at those positions.

It is worth mentioning that the two measures of the ultimate tensile strength of the HTPB sample under impact loading were obtained directly from our MD simulations. In this article, we refer to this as the direct method of measuring tensile strength. The values of these two ultimate tensile strengths cannot be acquired experimentally as it is impossible for researchers to place a sensor inside the material without altering its properties, even if the sensor is extremely small. Therefore, to facilitate comparison with experimental data, we also employ the spallation strength based on the acoustic assumption $(\sigma_{\rm spall,f1})$ and the modified acoustic assumption $(\sigma_{\rm spall,f2})$ to measure the ultimate tensile strength of HTPB materials under shock waves. $\sigma_{\rm spall,f1}$ and $\sigma_{\rm spall,f2}$ and the corresponding strain rate $\dot{\varepsilon}$ are defined as follows: $^{58-60}$

$$\sigma_{\text{spall},\text{f1}} = \frac{1}{2} \rho_0 C_b \Delta U_f \tag{7}$$

$$\sigma_{\text{spall},f2} = \frac{1}{2} \rho_0 (C_b - S\Delta U_f/2) \Delta U_f$$
(8)

$$\dot{\varepsilon} = \frac{\Delta U_{\rm f}}{2\Delta t} \frac{1}{C_{\rm b}} \tag{9}$$

In the equations, ρ_0 represents the initial density of HTPB, the pullback velocity ($\Delta U_{\rm f}$) corresponds to the difference between

the maximum and minimum values of the free surface velocity $(u_{\rm fs})$, and Δt denotes time.

3.4. Influence of Temperature on Spallation Fracture. Figure 7a demonstrates the changes of u_{fs} as functions of time under different impact velocities. As the shock front approaches the right edge (free surface) of the HTPB sample, its velocity rises from 0 to nearly twice the $U_{\rm I}$. Subsequently, the u_{fs} enter plateau phases and then gradually decline to the respective first minimum values. The decrease could be attributed to the energy dissipation caused by the collision of the reflected wave from the free surface and the release wave by the piston. The $\Delta U_{\rm f}$ is used to calculate the spallation strength by the indirect methods according to eqs 7 and 8. The time taken to decline from the maximum to the corresponding minimum value, denoted as Δt , is used to calculate the strain rate in eq 9. Figure 7b compares the four different spallation strengths under an initial temperature of 300 K with varying impact velocities. It is important to note that similar trends are also observed in other cases with different temperatures, which will be detailed later. We find that the criteria of $\sigma_{\text{spall,f2}}$ always yields the minimum values compared with other methods. The spallation strength calculated by $\sigma_{\text{spall,f2}}$ is very close to the counterparts obtained from σ_{FN} , with an average difference of $\pm 4.2\%$, due to the fact that in the case of $\sigma_{\rm spall,fl}$ it is assumed that only one spallation plane appears when the material fracture occurs. 60 Meanwhile, the defined fracture nucleation stress (σ_{FN}) exactly corresponds to the tensile stress of the initial spallation occurring. The only exception is in the case of $U_{\rm I}$ = 2.5 km/s at the lowest simulated impact velocity. The reason for this can be found in Figure 5a. At this $U_{\rm I}$ value, there is no obvious spallation plane appearing in the HTPB material, resulting in the value obtained directly through MD being relatively smaller than the actual spallation strength of HTPB.

Figures 7c and 7d display the changes of spallation strengths, obtained directly, from $\sigma_{T_{\rm max}}$ and $\sigma_{\rm FN}$ against the change of $U_{\rm I}$ and of the temperature. We find that $\sigma_{T_{\rm max}}$ and $\sigma_{\rm FN}$ share almost the same trend, with their values decreasing as $U_{\rm I}$ and temperature increase. As $U_{\rm I}$ and thus the input energy to the system increase, the local temperature rises as a result of the

shock front propagation; it causes the polymer chains within the HTPB to be more loosely distributed, thereby reducing the impact resistance of the HTPB material. A similar explanation can be applied to the decrease in the values of $\sigma_{T_{\rm max}}$ and $\sigma_{\rm FN}$ when the temperature is increased. Furthermore, a higher initial temperature corresponds to a higher spallation strength regardless of what criteria is used because at the lower temperature the rise of the temperature is limited locally such that the local structure is not as loose as the case with initial higher temperature. Within the simulated impact time, the degree of polymer chain looseness is far less than that at higher temperatures after complete relaxation. Note that at an initial temperature of 400 K with an $U_{\rm I}$ of 0.25 km/s, both $\sigma_{T_{\rm max}}$ and σ_{FN} have relatively small values and do not exhibit a continuous decline with increasing $U_{\rm I}$. This is because at the $U_{\rm I}$ of 0.25 km/s (see Figure 5a), no fracture in the HTPB material was observed within the simulated time range at 400 K. Lastly, we find that when the initial temperature of the model system is below the T_g , the spallation strength decreases monotonically as $U_{\rm I}$ increases, no matter what criteria are used. This significant decrease reflects that when the system temperature drops below $T_{\rm g}$, the spallation strength of HTPB noticeably increases. This can be attributed to the fact that below the $T_{\rm g}$, HTPB transitions from a liquid state to a solid state, enhancing its impact resistance.

Figures 7e and 7f present the spallation strengths calculated indirectly $(\sigma_{\text{spall},f1} \text{ and } \sigma_{\text{spall},f2})$ as functions of U_{I} and the temperature of HTPB. We find that $\sigma_{\text{spall,f1}}$ and $\sigma_{\text{spall,f2}}$ each exhibit two different trends, divided by the T_g . Above the T_g with the increase of $U_{
m I}$, the values of $\sigma_{
m spall,f1}$ and $\sigma_{
m spall,f2}$ display an initial increase, followed by a decrease and then an increase again. The initial increase might be due to the low $U_{\rm I}$ at the beginning, and because the HTPB is in a liquid state at this time, a large part of the energy input into the HTPB is dissipated during transmission. As a result, less energy is transferred to the free surface end from the spallation plane, resulting in a larger pullback velocity signal. The subsequent continuous decrease might be attributed to the increased system energy input with the increase in $U_{\rm I}$, leading to a greater number of spallation planes. This in turn reduces the energy transferred to the free surface end and lowers the pullback velocity signal. The increase in the final stage could be because at an U_1 of 1.5 km/s, HTPB has undergone complete fracture (see Figure 5a). The energy reduction caused by the emergence of the spallation plane has reached a threshold, and with the further increase of $U_{\rm L}$, more energy is transferred from the spallation plane to the free surface end, resulting in an increased pullback velocity signal. However, when the temperature drops below the $T_{\rm g}$, the values of $\sigma_{\rm spall,f1}$ and $\sigma_{
m spall,f2}$ exhibit a continuous decreasing trend with increasing $U_{
m I}$ This can be attributed to the fact that when the temperature falls below the T_g , the impact resistance and energy transfer efficiency of HTPB are improved. This implies a decrease in energy dissipation during propagation, while the energy required for complete fracture increases. This dual effect results in a continuous decrease in values $\sigma_{\text{spall,f1}}$ and $\sigma_{\text{spall,f2}}$ with the increase in $U_{\rm I}$ when the HTPB polymer is below the

 $T_{\rm g}$. **3.5. Comparison with Experimental Results.** Finally, we compare the results of the normal stress and the tensile strength obtained from our MD simulations with the available experimental results. Figure 8a presents the dependence of the

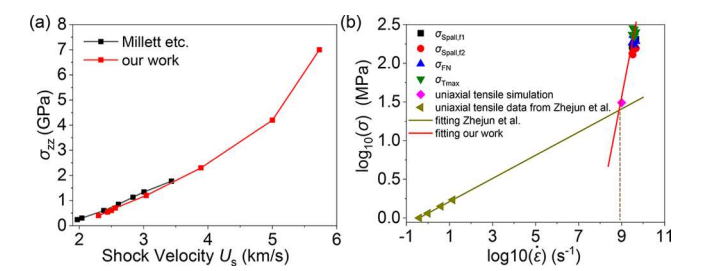


Figure 8. Comparison between our MD results of the normal stress with experimental data: ⁶¹ (a) the dependence of the tensile strength on the shock velocity; (b) comparison between the tensile strength with experimental data. ⁶¹ The magenta point is from the additional tensile simulation we performed.

normal stress on the shock velocities at an initial temperature of 300 K, comparing results determined by our MD simulations with data obtained by Millett et al. 25 through plate impact experiments. The normal stress obtained from our MD simulations closely matches the experimental data from Millett et al.²⁵ within the range of shock wave speeds between 2 and 3.5 km/s. Within this range, the normal stress and shock velocity are linearly correlated. In Figure 8b, we compare the spallation strengths according to the different criteria at 300 K with the experimental tensile strengths obtained by Wang et al.⁶¹ along with the corresponding strain rate. The plot reveals two distinct regimes. In the high-rate regime, covered by our estimations of the spallation strength, the low-rate regime is covered by the tensile experimental results. The strain rates corresponding to the spallation strength derived from our MD simulations are located approximately at the strain rate of 10¹⁰ s⁻¹, which is determined by eq 9. By fitting the results from the two regimes, we derive two intersecting linear lines. We performed an additional tensile simulation with a strain rate, 10⁹ s⁻¹, that corresponds to the intersection of the two lines The simulation predicted that the tensile strength approximately equals 30 MPa, which is consistent with the extrapolation. The stress-strain curve of the tensile simulation is illustrated in Figure S6. The discrepancy shown in Figure S8 is not surprising because previous research has demonstrated that strain rate has a notable influence on the mechanical behavior of polymers.⁶²

4. CONCLUSIONS

Results reveal that the changes in four different spallation strengths under various impact velocities are associated with the initial temperature of HTPB. The spallation strength calculated based on modified acoustic assumption always presents a minimum value, suggesting that the spallation strength calculated by this method is relatively conservative. The fracture nucleation stress and the maximum tensile stress both decrease as the $U_{\rm I}$ and temperature increase, while the spallation strength calculated based on the acoustic assumption $(\sigma_{\text{spall},fl})$ and the spallation strength calculated based on the modified acoustic assumption $(\sigma_{ ext{spall,f2}})$ demonstrate two distinct trends above and below the T_g . Above T_g , with the increase of $U_{\rm L}$, the values of $\sigma_{\rm spall,f1}$ and $\sigma_{\rm spall,f2}$ initially increase, then decrease, and finally increase again. Below the T_{g} , $\sigma_{\rm spall,fl}$ and $\sigma_{\text{spall},f2}$ only decrease with increasing simulated U_{I} . Besides, our study also demonstrates an increase in maximum normal stress with rising $U_{\rm I}$ and a decrease with higher initial temperatures. Notably, when the initial temperature is lower than the T_{σ} of HTPB, the temperature has a minimal impact on the maximum normal stress with the same $U_{\rm I}$. Finally, our results, when compared with experimental data, showcased reasonable accuracy, providing valuable molecular insights into the spallation behavior of HTPB under different conditions.

ASSOCIATED CONTENT

Data Availability Statement

To enhance the reproducibility of our results, we have made our simulation setup, simulation parameters, and postprocessing code publicly available in a public repository through GitHub. The database will be available at the repo https://github.com/yliu2397/Molecular-dynamics-simulations-of-shock-spallation-in-Hydroxyl-terminated-Polybutadiene-material upon the publishing of this work.

Supporting Information

The Supporting Information is available free of charge at https://pubs.acs.org/doi/10.1021/acsapm.3c01325.

Benchmarking—static and dynamic properties of *cis*-1,4-polybutadiene melts (specific volume, the total structure factor, intermolecular pair distribution function, mean-square end-to-end distance, and the characteristic ratio); strain—stress curve of uniaxial tensile with the strain rate of $1 \times 10^9 \, \mathrm{s}^{-1}$ and ensemble average mean-square radius of gyration (PDF)

AUTHOR INFORMATION

Corresponding Author

Ying Li — Department of Mechanical Engineering, University of Wisconsin—Madison, Madison, Wisconsin 53706, United States; orcid.org/0000-0002-1487-3350; Phone: +1 608-265-0577; Email: yli2562@wisc.edu; Fax: +1 608-890-3966

Authors

Yuhao Liu — Department of Mechanical Engineering, University of Wisconsin—Madison, Madison, Wisconsin 53706, United States; Oorcid.org/0009-0000-2037-9378

Jinlong He — Department of Mechanical Engineering, University of Wisconsin—Madison, Madison, Wisconsin 53706, United States

Weikang Xian – Department of Mechanical Engineering, University of Wisconsin—Madison, Madison, Wisconsin 53706, United States

Complete contact information is available at: https://pubs.acs.org/10.1021/acsapm.3c01325

Author Contributions

Y.L.: methodology, software, validation, formal analysis, data curation, writing—original draft, visualization. J.H.: methodology, software, formal analysis, data curation, writing—review and editing, visualization. W.X.: validation, methodology, software, writing—review and editing. Y.L.: conceptualization, methodology, software, writing—review and editing, supervision, project administration, funding acquisition.

Notes

The authors declare no competing financial interest.

ACKNOWLEDGMENTS

Y.L. thanks the support from the U.S. National Science Foundation (CMMI-2314424, CMMI-2316200, CAREER-2323108). Any opinions, findings, and conclusions or recommendations expressed in this material are those of the

authors and do not necessarily reflect the views of the U.S. National Science Foundation. The authors also acknowledge the National Renewable Energy Laboratory (Eagle Computing System) for providing HPC resources that have contributed to the research results reported within this paper. Support for this research was also provided by the University of Wisconsin—Madison, Office of the Vice Chancellor for Research and Graduate Education with funding from the Wisconsin Alumni Research Foundation.

REFERENCES

- (1) Vilar, W.; Akcelrud, L. Effect of HTPB structure on prepolymer characteristics and on mechanical properties of polybutadiene-based polyurethanes. *Polym. Bull.* **1995**, *35*, 635–639.
- (2) Brosse, J. C.; Derouet, D.; Epaillard, F.; Soutif, J. C.; Legeay, G.; Dusek, K. Hydroxyl-terminated polymers obtained by free radical polymerization-Synthesis, characterization, and applications. *Adv. Polym. Sci.* **1986**, *81*, 167–223.
- (3) Krishnan, P. S. G.; Ayyaswamy, K.; Nayak, S. K. Hydroxy Terminated Polybutadiene: Chemical Modifications and Applications. *J. Macromol. Sci. Part A-Pure Appl. Chem.* **2013**, *50*, 128–138.
- (4) Garcia, B. O.; Chavez, D. J. Shock compression of liquid hydrazine, 9th American-Physical-Society Topical Conference on Shock Compression of Condensed Matter; American Institute of Physics: Seattle, WA, 1995; pp 831–834.
- (5) Kanel, G. I.; Fortov, V. E.; Khishchenko, K. V.; Utkin, A. V.; Razorenov, S. V.; Lomonosov, I. V.; Mehlhorn, T.; Asay, J. R.; Chhabildas, L. C. Thin foil acceleration method for measuring the unloading isentropes of shock-compressed matter, 11th Conference of the American-Physical-Society-Topical-Group on Shock Compression of Condensed Matter; American Institute of Physics: Snowbird, UT, 1999; pp 1179–1182.
- (6) Yildirim, H. C.; Ozupek, S. Structural assessment of a solid propellant rocket motor: Effects of aging and damage. *Aerosp. Sci. Technol.* **2011**, *15*, 635–641.
- (7) Renganathan, K.; Sarma, B.; Rao, B. N.; Sivasubramonian, B.; Nair, N. J. Structural integrity assessment on a large solid booster propellant grain, 9th International Autumn Seminar on Propellants, Explosives and Pyrotechnics; Science Press Beijing: Nanjing, P. R. China, 2011; pp 443–453.
- (8) Zhuo, C. F.; Feng, F.; Wu, X. S. Development process of muzzle flows including a gun-launched missile. *Chin. J. Aeronaut.* **2015**, 28, 385–393.
- (9) Sui, X.; Wang, N. F.; Wan, Q. A.; Bi, S. H. Effects of relaxed modulus on the structure integrity of NEPE propellant grains during high temperature aging, Propellants Explos. *Pyrotech.* **2010**, *35*, 535–539.
- (10) Deng, B.; Xie, Y.; Tang, G. J. Three-dimensional structural analysis approach for aging composite solid propellant grains. *Propellants Explos. Pyrotech.* **2014**, *39*, 117–124.
- (11) O'Neil, P. T.; Heister, S. D. Evaluation of physical and ballistic properties of polymerized-dicyclopentadiene-based composite solid propellants. *J. Propul. Power* **2014**, *30*, 749–759.
- (12) Marimuthu, R.; Rao, B. N. Development of efficient finite elements for structural integrity analysis of solid rocket motor propellant grains. *Int. J. Pressure Vessels Pip.* **2013**, *111*, 131–145.
- (13) Sikder, A. K.; Sikder, N. A review of advanced high performance, insensitive and thermally stable energetic materials emerging for military and space applications. *J. Hazard. Mater.* **2004**, *112*, 1–15.
- (14) Badgujar, D. M.; Talawar, M. B.; Asthana, S. N.; Mahulikar, P. P. Advances in science and technology of modern energetic materials: An overview. *I. Hazard. Mater.* **2008**, *151*, 289–305.
- (15) Malhotra, P.; Jiao, T.; Henann, D. L.; Clifton, R. J.; Guduru, P. R. Dynamic shearing resistance of hydroxyl-terminated polybutadiene (HTPB). *J. Appl. Phys.* **2021**, *129*, 17.

- (16) He, Z. H.; Huang, Y. Y.; Ji, G. F.; Chen, J.; Wu, Q. Anisotropic reaction properties for different HMX/HTPB composites: A theoretical study of shock decomposition. *Molecules* **2022**, *27*, 2787.
- (17) Mahottamananda, S. N.; Kadiresh, P. Mechanical characteristics of paraffin wax-HTPB based hybrid rocket fuel, Proceedings of International Conference of Aerospace and Mechanical Engineering 2019: AeroMech 2019, 20–21 November 2019, Universiti Sains Malaysia, Malaysia; Springer: Malaysia, 2020; pp 91–103.
- (18) Sekkar, V.; Bhagawan, S. S.; Prabhakaran, N.; Rao, M. R.; Ninan, K. N. Polyurethanes based on hydroxyl terminated polybutadiene: modelling of network parameters and correlation with mechanical properties. *Polymer* **2000**, *41*, 6773–6786.
- (19) Jordan, J.; Montaigne, D.; Neel, C.; Sunny, G.; Molek, C. Shock and high strain rate characterization of HTPB with varying plasticizer, Annual Conference and Exposition of the Society-for-Experimental-Mechanics on Experimental and Applied Mechanics; Springer: Costa Mesa, CA, 2015; pp 39–42.
- (20) Chen, X. D.; Lai, J. W.; Chang, X. L.; Zhang, Y. H.; Zhang, L.; Wang, C. Compressive mechanical properties of HTPB propellant at low temperatures and high strain rates. *Results Phys.* **2017**, *7*, 4079–4084
- (21) Zhang, H. N.; Liu, M.; Miao, Y. G.; Wang, H.; Chen, T.; Fan, X. Z.; Chang, H. Dynamic mechanical response and damage mechanism of HTPB propellant under impact loading. *Materials* **2020**, *13*, 17.
- (22) Sunny, G. P. A high strain-rate investigation of a Zr-based bulk metallic glass and an HTPB polymer composite. Ph.D. Thesis, Case Western Reserve University, Cleveland, OH, 2011.
- (23) Yang, L.; Xie, K.; Pei, J. F.; Sui, X.; Wang, N. F. Compressive mechanical properties of HTPB propellant at low, intermediate, and high strain rates. *J. Appl. Polym. Sci.* **2016**, DOI: 10.1002/app.43512.
- (24) Frohlich, M. G.; Sewell, T. D.; Thompson, D. L. Molecular dynamics simulations of shock waves in hydroxyl-terminated polybutadiene melts: Mechanical and structural responses. *J. Chem. Phys.* **2014**, *140*, 12.
- (25) Millett, J. C. F.; Bourne, N. K.; Akhavan, J. The response of hydroxy-terminated polybutadiene to one-dimensional shock loading. *J. Appl. Phys.* **2004**, *95*, 4722–4727.
- (26) Yang, Y.; Wang, H. M.; Wang, C. Effects of the phase content on spallation damage behavior in dual-phase steel. *J. Mater. Eng. Perform.* **2021**, *30*, 5614–5624.
- (27) Du, Z.; Zhu, X. Y.; Li, F.; Zhou, S. Q.; Dai, Z. W. Failure of the asphalt-aggregate interface under tensile stress: Insight from molecular dynamics. *J. Mater. Civ. Eng.* **2021**, 33, 13.
- (28) DeVries, M.; Subhash, G.; Awasthi, A. Shocked ceramics melt: An atomistic analysis of thermodynamic behavior of boron carbide. *Phys. Rev. B* **2020**, *101*, 12.
- (29) Li, W. H.; Hahn, E. N.; Yao, X. H.; Germann, T. C.; Feng, B.; Zhang, X. Q. On the grain size dependence of shock responses in nanocrystalline sic ceramics at high strain rates. *Acta Mater.* **2020**, 200, 632–651.
- (30) Chen, J.; Fensin, S. J. Associating damage nucleation and distribution with grain boundary characteristics in Ta. *Scr. Mater.* **2020**, *187*, 329–334.
- (31) Wang, J. N.; Wu, F. C.; Wang, P.; He, A. M.; Wu, H. A. Double-shock-induced spall and recompression processes in copper. *J. Appl. Phys.* **2020**, *127*, *9*.
- (32) Plimpton, S. Fast parallel algorithms for short-range molecular dynamics. *J. Comput. Phys.* **1995**, *117*, 1–19.
- (33) Stukowski, A. Visualization and analysis of atomistic simulation data with OVITO-the Open Visualization Tool. *Model. Simul. Mater. Sci. Eng.* **2010**, *18*, 015012.
- (34) Sun, H.; Mumby, S. J.; Maple, J. R.; Hagler, A. T. An ab initio CFF93 all-atom force field for polycarbonates. *J. Am. Chem. Soc.* **1994**, 116, 2978–2987.
- (35) Heinz, H.; Lin, T. J.; Mishra, R. K.; Emami, F. S. Thermodynamically consistent force fields for the assembly of inorganic, organic, and biological nanostructures: the INTERFACE force field. *Langmuir* **2013**, *29*, 1754–1765.

- (36) Tow, G. M.; Maginn, E. J. Fully atomistic molecular dynamics simulations of hydroxyl-terminated polybutadiene with insights into hydroxyl aggregation. *Macromolecules* **2020**, *53*, 2594–2605.
- (37) Cui, J.; Hao, H.; Shi, Y. C.; Zhang, X. H.; Huan, S. Volumetric properties of concrete under true triaxial dynamic compressive loadings. *J. Mater. Civ. Eng.* **2019**, *31*, 10.
- (38) Jiang, Y. J.; Xue, J. S.; Chen, Z. J. Influence of volumetric property on mechanical properties of vertical vibration compacted asphalt mixture. *Constr. Build. Mater.* **2017**, *135*, 612–621.
- (39) Tsolou, G.; Harmandaris, V. A.; Mavrantzas, V. G. Temperature and pressure effects on local structure and chain packing in cis-1,4-polybutadiene from detailed molecular dynamics simulations. *Macromol. Theory Simul.* **2006**, *15*, 381–393.
- (40) Tsolou, G.; Mavrantzas, V. G.; Theodorou, D. N. Detailed atomistic molecular dynamics simulation of cis-1,4-poly(butadiene). *Macromolecules* **2005**, *38*, 1478–1492.
- (41) Dossi, E.; Earnshaw, J.; Ellison, L.; dos Santos, G. R.; Cavaye, H.; Cleaver, D. J. Understanding and controlling the glass transition of HTPB oligomers. *Polym. Chem.* **2021**, *12*, 2606–2617.
- (42) Zhou, Q. Z.; Jie, S. Y.; Li, B. G. Preparation of hydroxylterminated polybutadiene with high cis-1, 4 content. *Ind. Eng. Chem. Res.* **2014**, *53*, 17884–17893.
- (43) Fetters, L. J.; Lohse, D. J.; Richter, D.; Witten, T. A.; Zirkel, A. Connection between polymer molecular-weight, density, chain dimensions, and melt viscoelastic properties. *Macromolecules* **1994**, 27, 4639–4647.
- (44) Reed, E. J.; Fried, L. E.; Manaa, M. R.; Joannopoulos, J. D. A method for tractable dynamical studies of single and double shock compression, 13th Conference of the American-Physical-Society-Topical-Group on Shock Compression of Condensed Matter; American Institute of Physics: Portland, OR, 2003; pp 259–262.
- (45) Goldman, N.; Srinivasan, S. G.; Hamel, S.; Fried, L. E.; Gaus, M.; Elstner, M. Determination of a density functional tight binding model with an extended basis set and three-body repulsion for carbon under extreme pressures and temperatures. *J. Phys. Chem. C* **2013**, 117, 7885–7894.
- (46) Ju, Y. Y.; Zhang, Q. M.; Gong, Z. Z.; Ji, G. F.; Zhou, L. Molecular dynamics simulation of shock melting of aluminum single crystal. *J. Appl. Phys.* **2013**, *114*, 4.
- (47) Yang, X.; Zeng, X. G.; Pu, C. J.; Chen, W. J.; Chen, H. Y.; Wang, F. Molecular dynamics modeling of the Hugoniot states of aluminum. *AIP Adv.* **2018**, *8*, 11.
- (48) Xue, Q. Z.; Lv, C.; Shan, M. X.; Zhang, H. X.; Ling, C. C.; Zhou, X. Y.; Jiao, Z. Y. Glass transition temperature of functionalized graphene-polymer composites. *Comput. Mater. Sci.* **2013**, *71*, 66–71.
- (49) Simperler, A.; Kornherr, A.; Chopra, R.; Bonnet, P. A.; Jones, W.; Motherwell, W. D. S.; Zifferer, G. Glass transition temperature of glucose, sucrose, and trehalose: An experimental and in silico study. *J. Phys. Chem. B* **2006**, *110*, 19678–19684.
- (50) Dossi, E.; Akhavan, J.; Gaulter, S. E.; Williams, R. G.; Doe, W. J. Cross-linking of hydroxyl-terminated polyols with triethyleneglycol diglycidyl ether: An alternative to toxic isocyanates. *Propellants Explos. Pyrotech.* **2018**, 43, 241–250.
- (51) Bailey, E. J.; Winey, K. I. Dynamics of polymer segments, polymer chains, and nanoparticles in polymer nanocomposite melts: A review. *Prog. Polym. Sci.* **2020**, *105*, 26.
- (52) He, L.; Wang, F.; Zeng, X. G.; Yang, X.; Qi, Z. P. Atomic insights into shock-induced spallation of single-crystal aluminum through molecular dynamics modeling. *Mech. Mater.* **2020**, *143*, 12.
- (53) Dewapriya, M. A. N.; Miller, R. E. Molecular dynamics simulations of shock propagation and spallation in amorphous polymers. *J. Appl. Mech.-Trans. ASME* **2021**, *88*, 12.
- (54) Linder, C. J. University physics students' conceptualizations of factors affecting the speed of sound propagation. *Int. J. Sci. Educ.* **1993**, *15*, 655–662.
- (55) Li, W. H.; Hahn, E. N.; Yao, X. H.; Germann, T. C.; Zhang, X. Q. Shock induced damage and fracture in SiC at elevated temperature and high strain rate. *Acta Mater.* **2019**, *167*, 51–70.

- (56) O'Connor, T. C.; Elder, R. M.; Sliozberg, Y. R.; Sirk, T. W.; Andzelm, J. W.; Robbins, M. O. Molecular origins of anisotropic shock propagation in crystalline and amorphous polyethylene. *Phys. Rev. Mater.* **2018**, *2*, 16.
- (57) Trepl, T.; Schelter, I.; Kummel, S. Analyzing excitation-energy transfer based on the time-dependent density functional theory in real time. *J. Chem. Theory Comput.* **2022**, *18*, 6577–6587.
- (58) Dekel, E.; Eliezer, S.; Henis, Z.; Moshe, E.; Ludmirsky, A.; Goldberg, I. B. Spallation model for the high strain rates range. *J. Appl. Phys.* **1998**, *84*, 4851–4858.
- (59) Wang, X. X.; He, A. M.; Zhou, T. T.; Wang, P. Spall damage in single crystal tin under shock wave loading: A molecular dynamics simulation. *Mech. Mater.* **2021**, *160*, 8.
- (60) Antoun, T.; Curran, D. R.; Razorenov, S. V.; Seaman, L.; Kanel, G. I.; Utkin, A. V. Spallation in materials of different classes. *Spall Fracture* **2003**, 137–173.
- (61) Wang, Z. J.; Qiang, H. F.; Wang, G.; Huang, Q. Z. Tensile mechanical properties and constitutive model for HTPB propellant at low temperature and high strain rate. *J. Appl. Polym. Sci.* **2015**, *132*, 9.
- (62) Graziano, A.; Dias, O. A. T.; Petel, O. High-strain-rate mechanical performance of particle- and fiber-reinforced polymer composites measured with split Hopkinson bar: A review. *Polym. Compos.* **2021**, *42*, 4932–4948.



CAS BIOFINDER DISCOVERY PLATFORM™

BRIDGE BIOLOGY AND CHEMISTRY FOR FASTER ANSWERS

Analyze target relationships, compound effects, and disease pathways

Explore the platform

